Journal of Power Sources 237 (2013) 300–309

Contents lists available at SciVerse ScienceDirect

Journal of Power Sources

journal homepage: www.elsevier.com/locate/jpowsour

1 kW/1 kWh advanced vanadium redox flow battery utilizing mixed acid electrolytes

Soowhan Kim [a], Edwin Thomsen [a], Guanguang Xia [b], Zimin Nie [a], Jie Bao [a], Kurtis Recknagle [a], Wei Wang [a], Vilayanur Viswanathan [a], Qingtao Luo [a], Xiaoliang Wei [a], Alasdair Crawford [a], Greg Coffey [a], Gary Maupin [a], Vincent Sprenkle [a,*]

[a] Pacific Northwest National Laboratory, Richland, WA 99352, USA[1]
[b] UniEnergy Technologies, LLC, 4333 Harbour Pointe Blvd SW, Unit A, Mukilteo, WA 98275, USA

HIGHLIGHTS

- Advanced VRFBs with a mixed acid electrolyte was firstly demonstrated in a kW scale.
- The VRFB delivered >1.1 kW at 15–85% SOC range with high energy efficiency (82%).
- The VFRB operated continuously at >45 °C without any precipitation utilizing the mixed acid electrolytes.
- The VRFB might simplify system and reduce cost by eliminating heat exchanger.

ARTICLE INFO

Article history:
Received 8 December 2012
Received in revised form
13 February 2013
Accepted 15 February 2013
Available online 26 February 2013

Keywords:
Advanced vanadium redox flow battery
Redox flow battery
Stack
Efficiency

ABSTRACT

This paper reports on the recent demonstration of an advanced vanadium redox flow battery (VRFB) using a newly developed mixed acid (sulfuric and hydrochloric acid) supporting electrolyte at a kW scale. The developed prototype VRFB system is capable of delivering more than 1.1 kW in the operation range of 15–85% state of charge (SOC) at 80 mA cm^{-2} with an energy efficiency of 82% and energy content of 1.4 kWh. The system operated stably without any precipitation at electrolyte temperatures >45 °C. At similar electrolyte temperatures, tests with a conventional sulfuric acid electrolyte suffered from precipitation after 80 cycles. By operating stably at elevated temperatures (>40 °C), the mixed acid system enables significant advantages over the conventional sulfate system, namely; 1) high stack energy efficiency due to better kinetics and lower electrolyte resistance, 2) lower viscosity resulting in reduced pumping losses, 3) lower capital cost by elimination of heat exchanger, 4) higher system efficiency and 5) simplified system design and operation. Demonstration of the prototype stack with the mixed acid electrolyte has been shown to lower the cost of conventional VRFB systems for large-scale energy storage applications.

1. Introduction

The demand for large-scale electrical energy storage (EES) devices has been growing for both improved efficiency and flexibility of the current grid infrastructure and to enable a higher penetration of stochastic renewable sources such like solar and wind onto the grid. Among the most promising technologies for the grid-scale EES are redox flow batteries (RFBs), which are capable of storing a large quantity of electricity (multi-MWs/MWhs) in a relatively simple and straightforward design [1,2].

There are several RFB technologies including polysulfide/bromide [3,4], all vanadium [5–8], Fe/Cr [9], and etc [2], however, the all-vanadium redox flow battery (VRFB) has received significant attention because of its excellent electrochemical reversibility, high round-trip efficiency, and negligible cross-contamination between positive and negative electrolytes [10]. Systems up to multi-MWs have been demonstrated for grid applications and renewable integration [10].

Even though the VRFB technology has several advantages over the conventional Li ion or lead acid batteries, high capital cost is one

* Corresponding author. Tel.: +1 509 375 2370; fax: +1 509 375 2186.
E-mail address: vincent.sprenkle@pnnl.gov (V. Sprenkle).

[1] PNNL is a multiprogram laboratory operated by Battelle Memorial Institute for the Department of Energy under Contract DE-AC05-76RL01830. Use of specific brands or trademarks is for research purpose only and does not constitute an endorsement.

0378-7753/$ – see front matter © 2013 Elsevier B.V. All rights reserved.
http://dx.doi.org/10.1016/j.jpowsour.2013.02.045

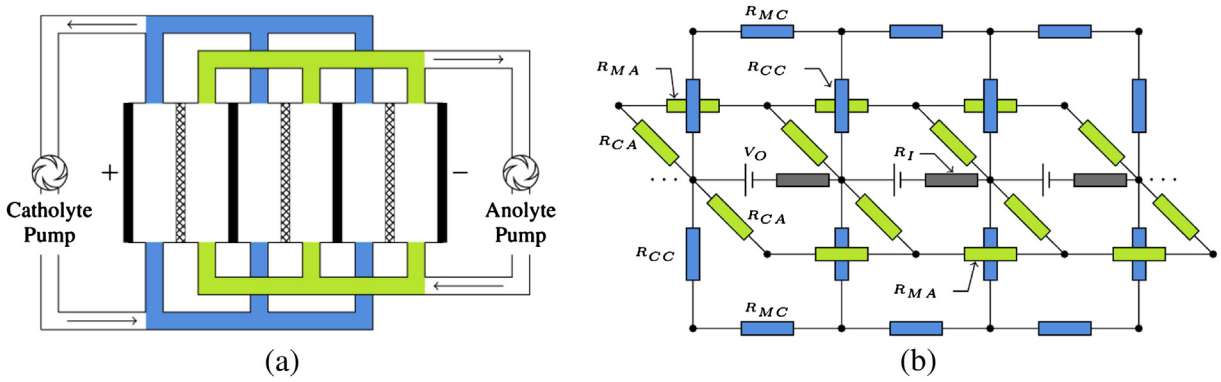

Fig. 1. (a) Schematic of a redox flow cell stack assembly, and (b) equivalent electric circuit model. R_{MC} and R_{CC} denote resistances of manifold and channel for catholyte, respectively. R_{MA} and R_{CA} denote resistances of manifold and channel for anolyte, respectively. V_O and R_I denote open circuit voltage and internal cell resistance, respectively.

major challenge for the widespread deployment of VRFB's. The high cost of these systems can be attributed to several factors, including the use of expensive vanadium, costly Nafion membrane and the need of an additional heat exchanger system to help maintain the electrolyte temperature between 25 and 35 °C in order to prevent precipitation of the conventional pure sulfate electrolyte.

Recently, PNNL scientists [11] made a dramatic improvement in the thermal stability and solubility of the conventional pure sulfate VRFB system by developing a mixed acid (hydrochloric and sulfuric acid) supporting electrolyte. In small-scale, single flow cell tests, electrolytes with up to 2.5 M vanadium in the mixed acid electrolyte (vs. <1.6 M for the conventional VRFB) demonstrated stable charge/discharge cycling operation over a temperature range of −5 ∼ 50 °C. In addition to the increased concentration, the addition of chloride ions also reduced the viscosity of the electrolyte [12], potentially reducing the power consumption required for pumping the electrolyte through the cell.

Despite the exceptional advantages of the advanced VRFB system, demonstration of the technology in a larger, kW scale stack was considered to be critical in order to validate the technology and avoid any potential risks that may not be easily observed in a lab-scale, single cell tests. To complete validation of the mixed acid technology, we recently developed and demonstrated a 1 kW/1 kWh scale prototype stack and system. This demonstration will help identify and mitigate potential challenges prior to scale up of the technology to MW grid scale applications. In this paper, we will report on the modeling, design, construction and performance of a kW scale stack and system as well as a brief component cost estimate.

2. Shunt current analysis and fluid flow model

Within the operating redox flow battery, shunt currents can develop which will reduce the overall efficiency of the battery. In the stack, bipolar plates, porous electrodes, flow field plates, and membranes are connected in a series configuration in order to develop the voltage required. The anolyte and catholyte are supplied by external tanks and are distributed to each level of the stack by a common manifold. With this configuration a leakage, or shunt current, can develop within the anolyte and catholyte flow paths due to the conductivity of the electrolytes. The shunt current is dependent upon several factors including; the number of cells in the stack, the potential gradient across the stack, and the overall design of the flow field. One of the most effective methods to reduce the shunt current is accomplished by increasing the electrolyte resistance along the flow path (e.g. high channel resistance). While effective for reducing shunt current, this approach greatly increases the pressure drop in the flow channel, thereby increasing

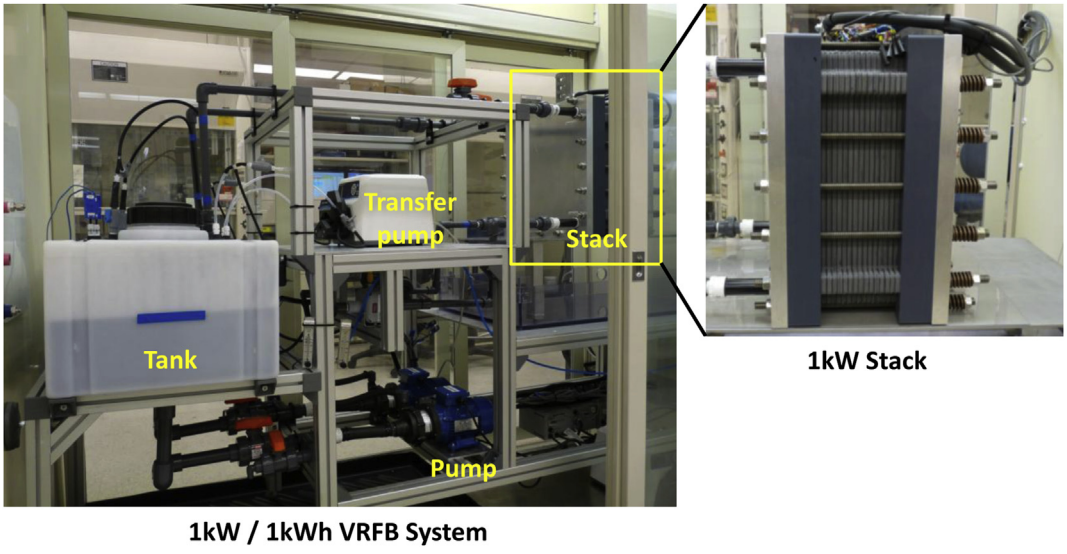

Fig. 2. 1 kW/1 kWh VRFB system and 1 kW stack.

the power required for the pumps. Thus, a trade-off design is required to optimize the flow channels within the flow frames.

In order to model the shunt current in the kW level, an electrical circuit analogy model [13,14] was used. Fig. 1 shows the schematic flow cell stack assembly and the representative electrical circuit model. The solution methodology for the shunt current model has been described in Ref. [14].

The shunt current model and flow analysis used the following baseline assumptions:

- Flow frames and manifolds are non-conductive.
- There is negligible potential gradient on the electrode surface.
- Cells are assumed as an ideal voltage source, represented by open circuit voltage and internal resistor.
- Cross-diffusion of vanadium ions is neglected.
- Electrolyte conductivity is assumed 0.2 Ω^{-1} cm^{-1}.
- Internal cell resistance is 1.0 Ω cm^2.

Fluid flow in the stack was modeled using a commercial computational fluid dynamics (CFD) package of STAR-CD (version 4.14, CD-Adapco). The fluid is assumed an incompressible, steady, single phase, and isothermal. In the domain of the flow channel and manifold, incompressible mass and momentum conservation equations were solved, while in the porous electrode, the momentum equation was replaced with Darcy flow equation:

$$\nabla \cdot u = 0 \tag{1}$$

$$u \cdot \nabla u = -\frac{1}{\rho}\nabla p + \frac{\mu}{\rho}\nabla^2 u \tag{2}$$

$$-\frac{\mu}{k}v = \nabla p \tag{3}$$

where u is the velocity vector, p is the pressure, and ρ is the density (assumed 1400 kg m^{-3}), μ is the dynamic viscosity (assumed 0.006 kg m^{-1} s^{-1}), v is the superficial velocity, and k is permeability of the porous electrode (assumed 1.685×10^{-10} m^2). The property of the porous electrode is also assumed isotropic.

Shunt current analysis and CFD models were employed to determine both the shunt current and the pressure drop associated with various stack designs. The final design went through multiple iterations before a suitable trade-off between pressure drop and shunt current was found.

3. Experimental

3.1. Chemicals

$VOSO_4 \cdot xH_2O$ (Noah Technologies, San Antonio, TX, 99.5%, $x = 2.0–2.3$), HCl (Sigma–Aldrich, 37%) and H_2SO_4 (Sigma–Aldrich, 95.8%) were used without further purification to fabricate both a pure sulfate electrolyte solution (1.5 M V + 3.5 M S) and a mixed acid electrolyte (2 M V + 2 M S + 5 M Cl).

Table 1
Specification of 1 kW class stack.

Dimension (cm)	31 (W) × 44 (H) × 40 (L)
Active area (cm^2)	780
Number of cells	15
Electrode	Graphite felt (SGL GFD4.6) SIGRACET® expanded graphite (TF6)
Flow frame	PVC (polyvinyl chloride)
Membrane	Nafion® 115
End plate	Aluminum plate
Power @ 80 mA cm^{-2}	>1.1 kW
DC roundtrip energy efficiency @ 80 mA cm^{-2}	>80%

3.2. 1 kW/1 kWh VRFB test system

Prior to fabrication of 1 kW/1 kWh VRFB test system, a 3 cell stack was fabricated to validate the stack component design including the flow field plate, seals and compression fixture. The compression fixture includes PVC end plates, aluminum end plate, tin-coated copper current collector plates, bolts and compression springs. A new integrated cell design combines the anode and cathode flow frame plates, a thin solid graphite plate (SGL expanded graphite, TF6), two porous graphite felts (SGL, GFD4.6) into a single component, which can significantly reduce the cost while improving reliability and sealing. Each flow frame plate, shown in Fig. 3a, includes five guide channels (32 cm effective length with 3 mm width and 1 mm depth). Each channel is connected to a common buffer layer (5 mm wide, 300 mm long and 1 mm deep) and diffusers prior to felt electrodes. The graphite felt porous electrode was compressed by 15% and prior to the assembly, thermally heat-treated in air at 400 °C for 6 h to enhance electrochemical activity and hydrophilicity. Nafion® 115 membrane was used and was soaked in deionized water for more than 24 h prior to the stack assembly. Based on the results of the 3 cell stack, a 1 kW class prototype stack (Fig. 2) with 15 repeat unit cells was fabricated using the same components and assembly process. Specifications for the 1 kW stack are summarized in Table 1.

Stack performance was measured using an in-house designed test system. Two test systems were fabricated; 1) 1 kWh for 1 kW stack (Fig. 2) and 2) 200 Wh for the 3-cell stack (not shown here). The test system includes one stack, two electrolyte reservoir tanks, two main centrifugal pumps (Finnish Thomson, DB4V-T-M613), two flow meters, pressure sensors (Measurement Specialties MSP-300-100-P-1-N-1), temperature sensors, one transfer pump, and valves. Both systems have the same configuration except for different specifications on the flow meters and electrolyte tanks. The flow meter for the 1 kW/1 kWh system was selected to allow for high flow rate with low pressure drop (FMG83-FKM, Omega Engineering, Inc.), while the FMG82-FKM model (Omega Engineering, Inc) was chosen for the 3 cell-stack system. For the 1 kW/1 kWh system, 30 L each of anolyte and catholyte was used and contained in a 45 L tank made from high density polyethylene (HDPE). 9 L tanks were employed for the 3 cell stack system. In addition to supply and return ports, each tank is equipped with four ports for pressure and temperature sensors, one transfer line, and one nitrogen purge. 1/8″ Teflon coated type N thermocouple was inserted inside each tank to measure the electrolyte temperature. Two tanks were connected by ¼″ tube to maintain equal pressure between the tanks. This helped avoid mechanical pressure variations attributed to the electrolyte volume change as a result of ionic or water transport across the membrane of the stack. To measure the pressure drop, one pressure transducer was located between the pump and stack inlet on both the anode and cathode side. 1″ PVC pipe was used from tank supply port to pump inlet while ½″ PVC pipe was used otherwise.

Charge/discharge cycling performance was evaluated using a battery tester (Arbin Instruments, BT-2000). Individual cell voltages and sensors including the flow meters, thermocouples and pressure transducers were monitored by the Arbin battery tester. The flow rate was varied and controlled by feedback PID control of the Arbin through an in-house designed speed controller. The system was purged by nitrogen and sealed prior to charge/discharge cycling to prevent oxidation of active species by air. The flow battery was cycled between 1.65 and 1.2 V per cell at 80 mA cm^{-2} at different flow rates. Additional performance at was measured at

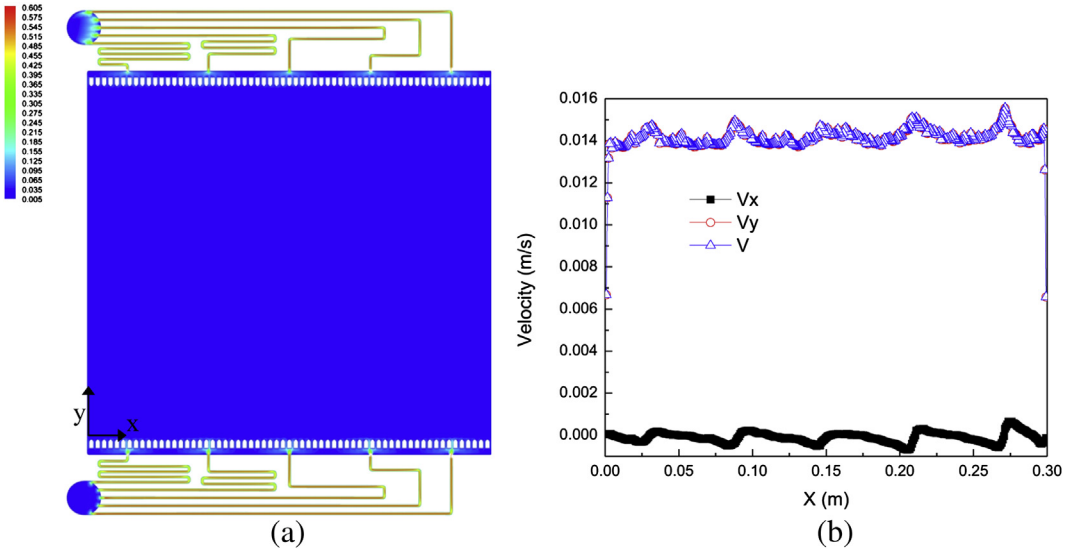

Fig. 3. (a) Velocity field at 1 mL min^{-1} cm^{-2} $cell^{-1}$ and (b) velocity distribution along the *x* direction near the felt tip, indicating uniform plug flow.

comparable flow rates and 160 mA cm^{-2} while being cycled between 1.75 and 1.1 V per cell. The difference in voltage ranges is to compensate for the different ohmic losses and ensure the state of charge (SOC) range of both tests is between 15 and 85%.

Efficiencies and pumping power are defined as:

$$\text{Stack coulombic efficiency (CE)} = \frac{\int i_d dt}{\int i_c dt} \tag{4}$$

$$\text{Stack energy efficiency (EE)} = \frac{\int p_d dt}{\int p_c dt} = \frac{\int V_d i_d dt}{\int V_c i_c dt} \tag{5}$$

$$\text{System energy efficiency} = \frac{\int \left(p_d - p_{\text{pump}}\right) dt}{\int \left(p_c + p_{\text{pump}}\right) dt} \tag{6}$$

$$p_{\text{pump}} = \frac{Q\Delta p}{\eta} \tag{7}$$

where *i* denotes current, *p* is power, *V* is voltage, subscripts of *c*, *d*, and pump denote charging, discharging and pump, respectively. *Q* is the flow rate, Δp is pressure drop, and η is the efficiency of the pump and motor (assumed to be 0.5 for the system).

Anolyte and catholyte were totally remixed and charged prior to each test to ensure identical initial test conditions in order to make accurate comparisons between the different test sets. Prior to remixing, electrolytes were deep discharged to 0.8 V per cell at a flow rate of 6 L min^{-1} and 80 mA cm^{-2} to minimize heat generation.

4. Results and discussion

4.1. CFD modeling and shunt current analysis

CFD analysis on a single flow frame, Fig. 3, shows that the final flow frame design has very uniform electrolyte flow distribution even at a high flow rate of 1 mL min^{-1} cm^{-2} $cell^{-1}$, which is a key requirement of the stack design. The CFD modeling parameters used in this analysis were: a permeability of 1.685×10^{-10} m^2 at a 15% compression of the graphite felt electrode, an electrolyte viscosity of 6 cP with a density of 1.4 g cm^{-3}. Both the viscosity and density were measured at an ambient temperature using the conventional electrolyte (1.7 M V (VI) + 5 M S). With these values, a total pressure drop of 99 kPa was predicted at a flow rate of 0.5 mL min^{-1} cm^{-2} $cell^{-1}$ with the porous electrode dominating the total pressure drop (~70% of total pressure drop).

In addition to the uniform flow distribution in the porous electrode, uniform flow distribution to each cell is of great importance in the stack design. CFD analysis on 20 and 40 cell stacks with the same flow frame design was conducted for the counter flow configuration with the inlet and outlet ports on the same end plate. As the number of cells increase, cells near the ports tend to have slightly larger flows, but the maximum variation is less than 0.25% of the ideal flow rate (Fig. 4). CFD analysis confirmed that this flow frame design enabled uniform fluid flow in both 20 and 40 cell stack assemblies.

Fig. 5 shows the shunt loss predicted for a 20-cell stack with this current flow frame design and properties of the 1.5 M V(VI) + 5 M S solution (less than 0.5% of load current). During charge, shunt current reduces the actual cell current available for electrochemical reactions, while during discharge, actual cell currents are increased due to the shunt current. For a single cell, coulombic efficiency (CE) was less than 100% as a result of transport of active species across the membrane. For stack configurations, the CE will be further reduced by the additional shunt current losses. Given the operation range of 20–80% SOC, the CE in the 20 cell stack was estimated to be ~1% lower than that in the single cell.

In conclusion, the CFD and shunt current analyses confirmed that the flow frame design (Fig. 3a) was appropriate to build a 1 kW prototype stack with low shunt and pressure losses.

4.2. Charge/discharge performance of flow battery

Fig. 6 compares charge/discharge voltage and power at 80 and 160 mA cm^{-2} and a flow rate of 6 L min^{-1} for the prototype 15-cell stack with the mixed acid electrolyte. The voltage differential between two different current conditions was almost the same during the entire operation range indicating the voltage drop is dominated by ohmic loss. At a constant current discharge of 80 mA cm^{-2}, the

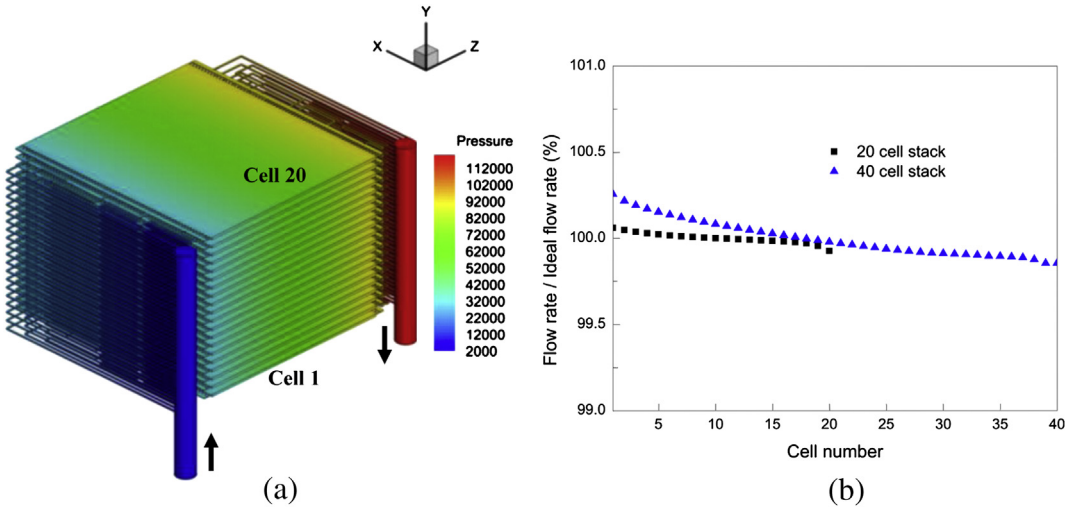

Fig. 4. (a) Pressure field at 0.5 mL min^{-1} $cell^{-1}$ cm^{-2} and (b) flow rate distribution in the stack.

minimum power the stack delivered was 1.12 kW at the end voltage of 18 V. The average power was 1.24 kW and the average energy efficiency was 82%. In comparison, the continuous power of the stack doubled (average power of 2.34 kW) at 160 mA cm^{-2} at the expense of energy efficiency (74%).

Flow rate is an important operational parameters that will affect performance as well as pumping power consumption in the flow battery. Fig. 7a compares the charge/voltage curves at different flow rates and different current densities. Lowering the flow rates drastically reduced capacity as well as energy content rather than the energy efficiency. For example, the discharge energies at 4 and 2 L min^{-1} are, respectively 96 and 83% of that at 6 L min^{-1} and 80 mA cm^{-2}, while the energy efficiencies are 99 and 97% of that at 6 L min^{-1}. This trend is more conspicuous at 160 mA cm^{-2} where the discharge energies at 4 and 2 L min^{-1} were reduced by 11 and 37%, respectively compared to that at 6 L min^{-1} while the energy efficiencies decreased by only 2 and 6%. This observation is consistent with the literature [15] and may be attributed to higher mass transport overpotentials at the lower flow rates, especially at high current densities.

The higher flow rates decreased mass transport losses, thereby improving the stack performance, as evidenced in the low charging and high discharging voltages (Fig. 7a), by decreasing the effective ionic transport distance [16]. However, the higher flow rates result in increased power for the pumps. Thus optimal operation for maximum system energy efficiency involves a trade-off between electrochemical performance and pumping losses.

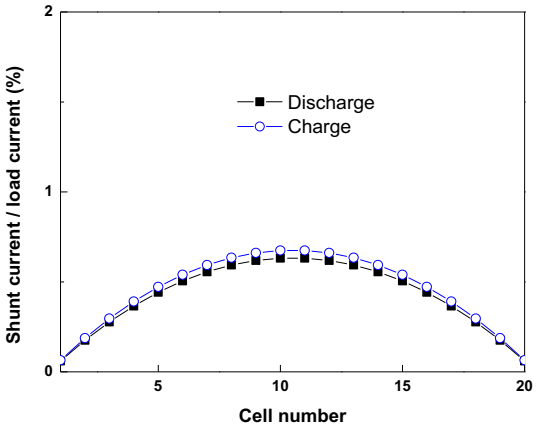

Fig. 5. Prediction of shunt current distribution in the 20 cell stack at 50 mA cm^{-2} and SOC 80%.

Pumping power consumption was estimated using Equation. (7) and assuming an efficiency of 50% for the pump and motor as shown in Fig. 7c. The pressure drop in the stack increased linearly with the flow rate resulting in quadratic increase of the required pumping power with the flow rate. At 80 mA cm^{-2}, the stack electrochemical energy efficiency increased with flow rate (Fig. 7d), while the system efficiency peaked around 4 L min^{-1}, because at greater flow rates, the pumping loss dominates the cell performance gain associated with enhanced mass transport. In comparison, at 160 mA cm^{-2}, both the stack and system efficiencies continuously increase with flow rate since the mass transport losses dominate the pump losses at higher currents.

The optimum system efficiency at 80 mA cm^{-2} was obtained at flow rate around 0.34 mL min^{-1} cm^{-2} $cell^{-1}$ (4 L min^{-1}), while a flow rate $>$ 0.5 mL min^{-1} cm^{-2} $cell^{-1}$ (6 L min^{-1}) was determined to be optimum at 160 mA cm^{-2}. It should be noted that our test was conducted at a constant flow rate for each test set. In order to further improve the system efficiency, a variable flow rate should be adopted based on several factors including SOC, current and direction of current (whether the system is being charged or discharged). Future research efforts will focus on this task.

Fig. 8a shows the cyclic performance of the 1 kW/1 kWh prototype system operated at ambient temperature without any external thermal management system. The coulombic and energy efficiencies remain constant over the varied test conditions, indicating that this prototype system is capable of operating reliably. Fig. 8b shows that without any external heat management system, the electrolyte temperature reached between 35 and 40 °C at 80 mA cm^{-2} and 45–49 °C at 160 mA cm^{-2}. It is important to note that even at these elevated temperatures, the prototype system utilizing the mixed acid electrolyte was able to deliver reliable power and energy without any precipitation. Validation of this mixed acid system in the kW scale system without any external heat exchanger systems demonstrates its distinct advantages over the conventional pure sulfate system.

Fig. 9 compares the coulombic and energy efficiencies of a 3 cell and 15 cell stack under the same operating conditions. The coulombic efficiency of the 15 cell stack was 95%, 1.7% lower than that of the 3 cell stack, 96.7%. Both stacks were cycled between 15 and 85% SOC at 80 mA cm^{-2}. The averaged electrolyte temperature

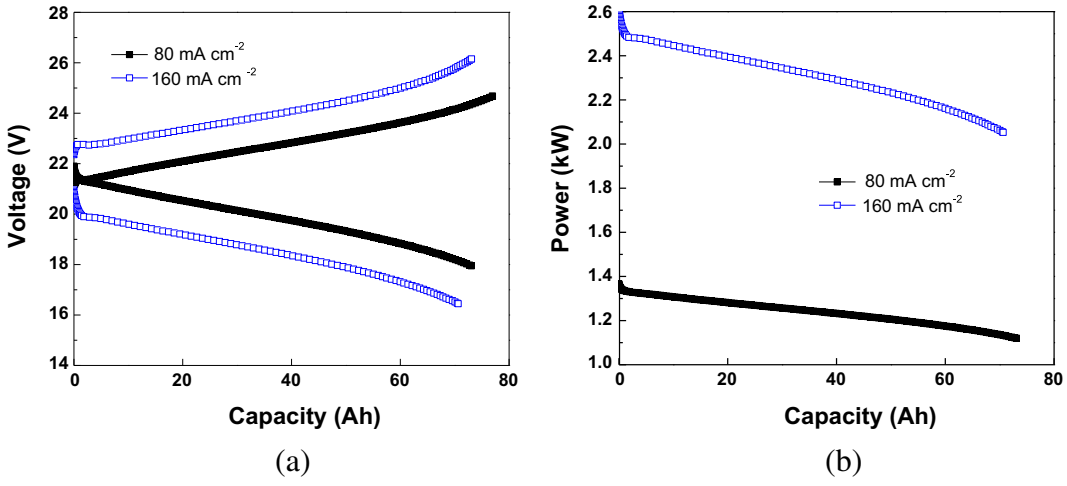

Fig. 6. Charge and discharge performance of the 15 cell-stack with the mixed acid electrolyte at 80 and 160 mA cm^{-2} and flow rate of 6 L min^{-1}: (a) charge and discharge curves and (b) discharge power curves.

was about 38 °C for both. The decrease in CE between the 3 cell and 15 cell stack is due to the increased shunt current losses for the larger stack.

One of the most important design criteria for the stack assembly is for it to have minimal performance variation from cell to cell. Performance variations between cells manifest themselves as variation in cell voltage during charge or discharge. Fig. 10 shows that the variation in cell voltage was minimal during the entire charging period at the two different current densities, 80 and 160 mA cm^{-2} even at lower than optimal flow rates (2 and 4 L min^{-1}). This indicates that the flow distribution in the stack is quite uniform, as predicted by the CFD analysis. In addition, other

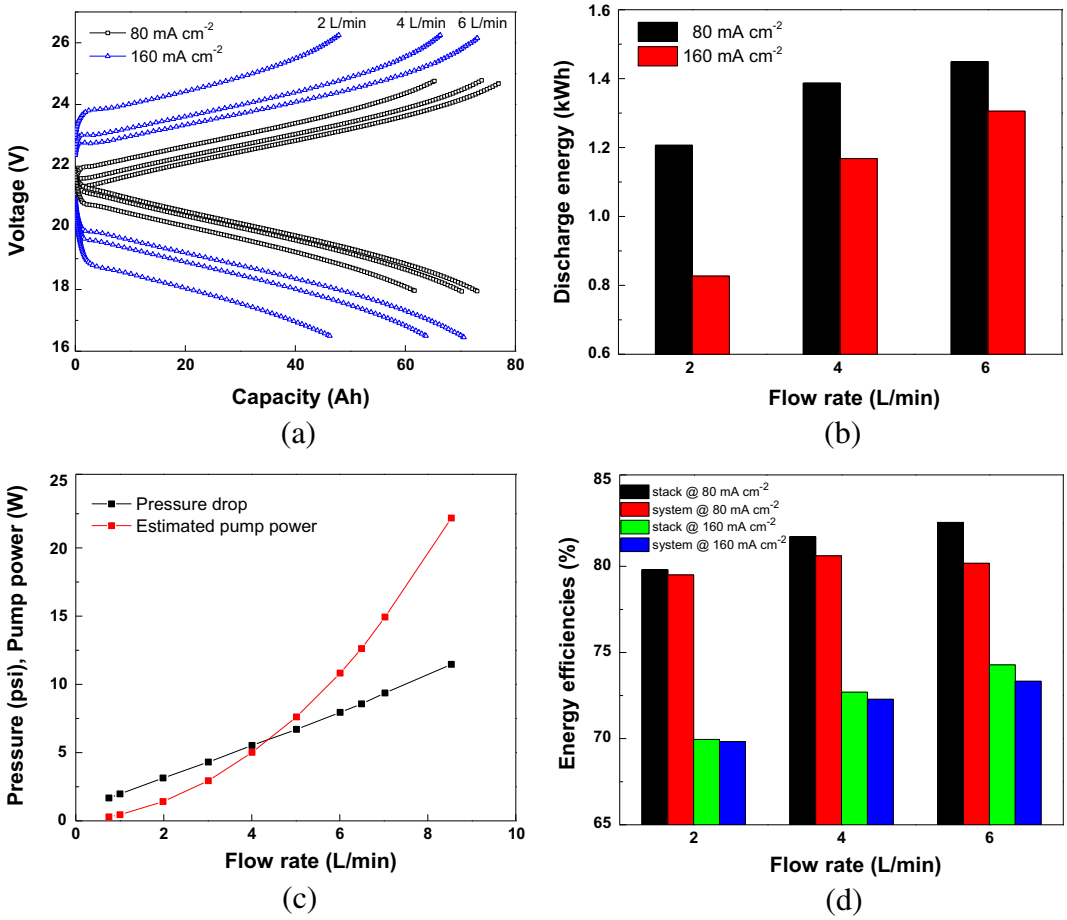

Fig. 7. Effect of flow rates and current densities on performance and efficiencies of the 15 cell-stack with the mixed acid electrolyte: (a) voltage behaviors, (b) discharge energy, (c) pressure drop and pumping power, where the electrolyte temperature was 33 °C and the SOC was ~15% when measured, and (d) stack and system efficiencies.

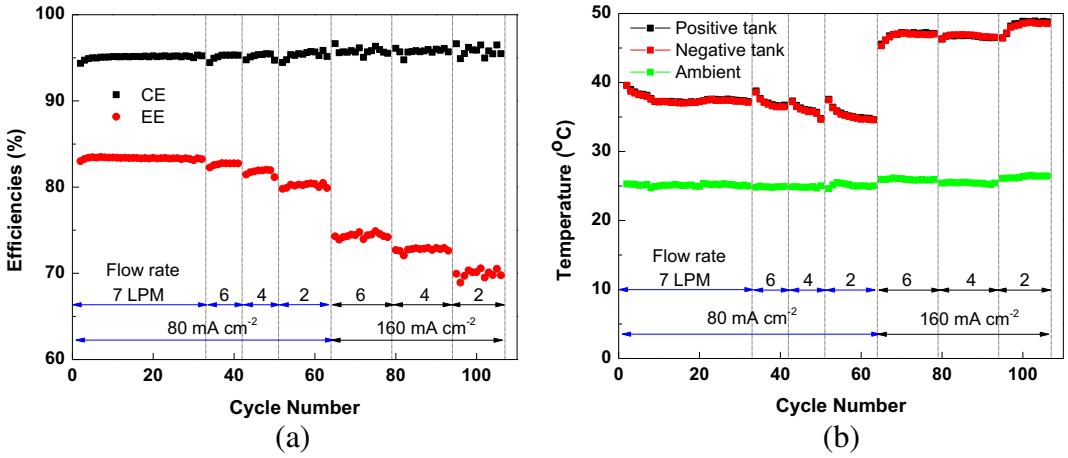

Fig. 8. a) Cyclic performance of the 15-cell stack with the mixed acid electrolyte. b) Operating temperature of 15-cell stack with mixed acid electrolyte.

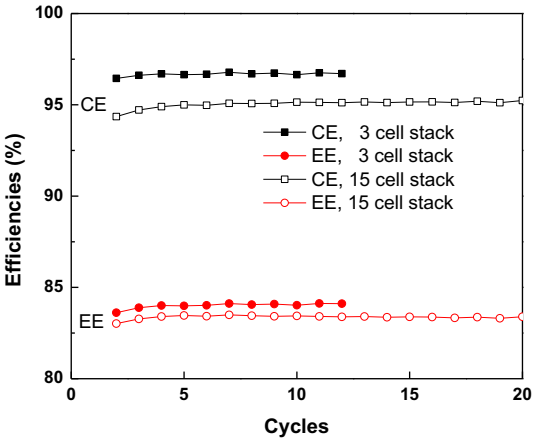

Fig. 9. Comparison of coulombic and energy efficiencies of 3-cell stack and 15-cell stack with the mixed acid electrolyte at 80 mA cm^{-2}.

losses like ohmic resistance and activation polarization are assumed to be quite uniform from cell to cell given the observed uniformity in performance. At the mid-point of charge (50% SOC), the standard deviation of the cell voltages were 1.5 and 2.3 mV at 80 and 160 mA cm^{-2}, respectively, while at the end of charge, the variation increased slightly to 3 and 5.7 mV at 80 and 160 mA cm^{-2}, respectively.

4.3. Comparison of cyclic stability between conventional and new mixed acid systems

Fig. 11 compares the operational reliability of two different electrolytes, pure sulfate and mixed acid, using the 3 cell stack configuration. The 3 cell stack with the conventional sulfate electrolyte was cycled at 80 mA cm^{-2} and 0.75 L min^{-1}, while the stack with our new mixed acid electrolyte was cycled at a more severe condition corresponding to160 mA cm^{-2} and 1.5 L min^{-1}, with associated higher operating temperature. Even at the elevated temperature of ~43 °C, the mixed acid system demonstrated stable cyclic efficiencies and inlet pressures, while the conventional system showed a slight decrease in the voltage efficiency after the 80th cycle (Fig. 11d). The decrease in voltage efficiency was accompanied by a dramatic increase in the stack inlet pressure at the positive side (Fig. 11f). The reason for performance degradation was obvious from the postmortem analysis (Fig. 12), which showed that precipitation took place inside the positive felt electrode as a result of the limited solubility of V^{5+} at the elevated temperature. It should be noted that the red color in web version in the positive electrode is evidence of V_2O_5 solid particles.

As evidenced in our previous work on small 10 cm [2] cell tests [11], the current kW scale system with the mixed acid electrolyte demonstrated stable operation without any precipitation at elevated temperatures. This advantage of the mixed acid electrolyte will simplify the system design, leading to higher system efficiency and a reduction in the system cost. Another system advantage of the mixed acid electrolyte is a lower pressure drop that will reduce

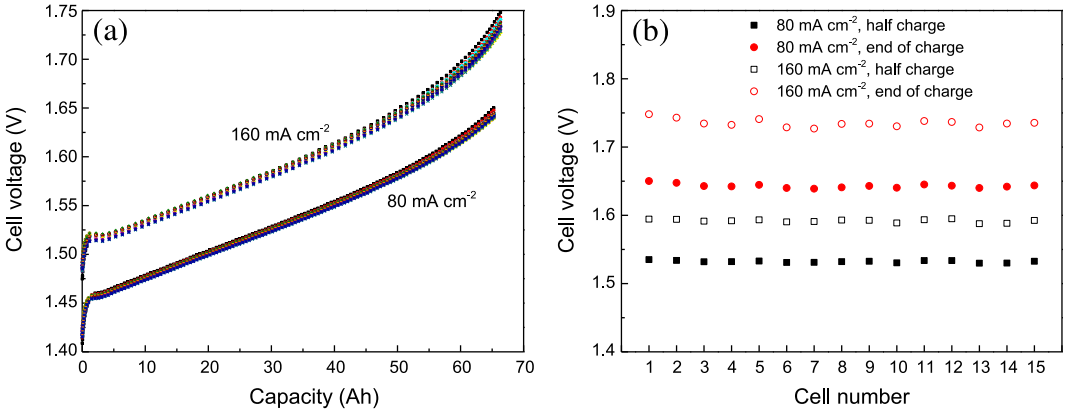

Fig. 10. Cell voltage variation of the 1 kW stack: (a) charge voltage at current densities of 80 and 160 mA cm^{-2} where the flow rate is 2 and 4 L min^{-1}, respectively, and (b) cell voltages at mid and end of charge in (a).

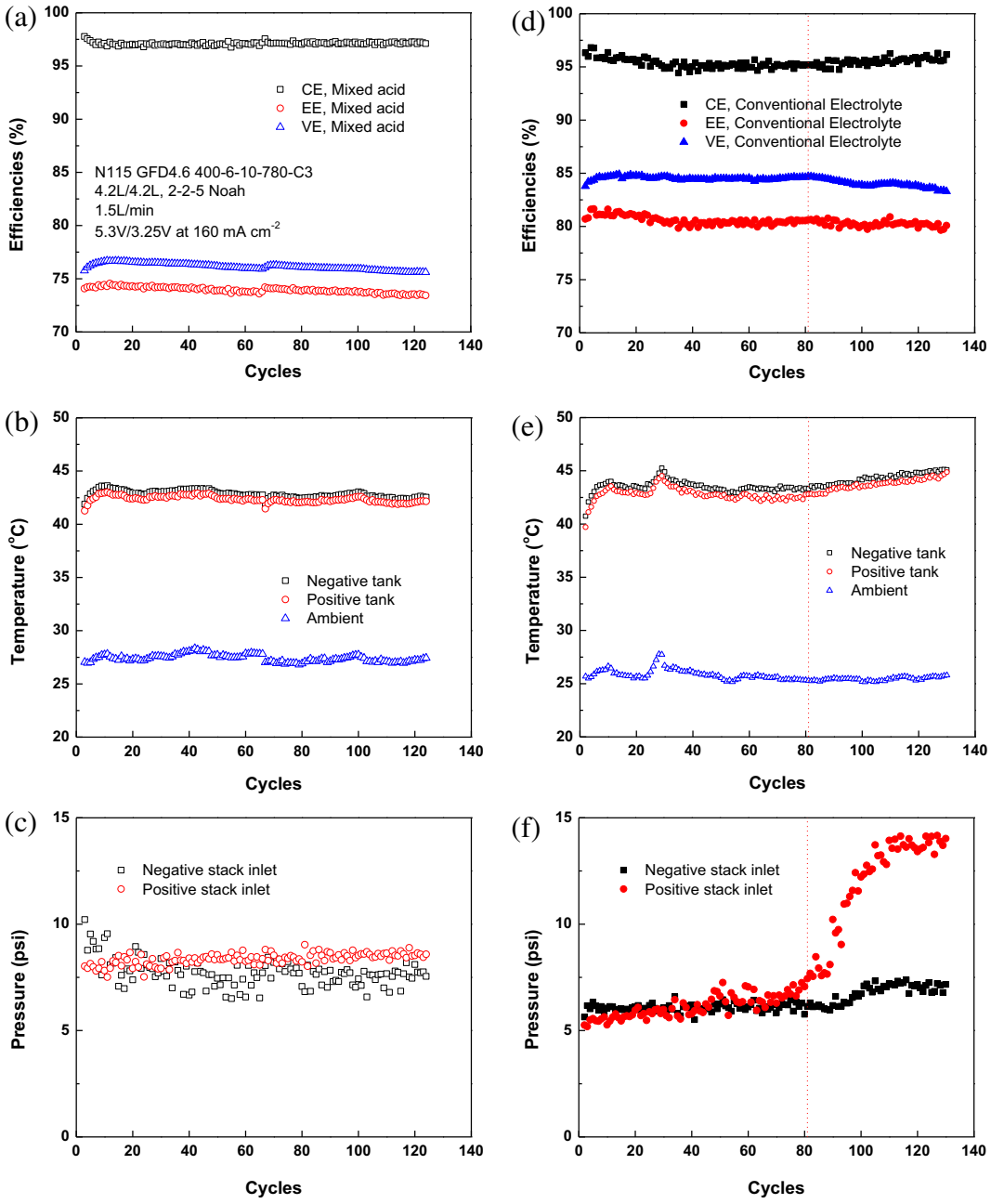

Fig. 11. Comparison of operational reliability of mixed acid and conventional electrolytes: 3 cell stack of the conventional electrolyte was cycled between 10 and 90% SOC at 80 mA cm^{-2}, flow rate of 0.75 L min^{-1}, and electrolyte volume of 2 L/2 L. The 3 cell stack of the mixed electrolyte was cycled between 10 and 90% SOC at 160 mA cm^{-2}, flow rate of 1.5 L min^{-1}, and electrolyte volume of 4.2/4.2 L. (a), (b), and (c) for the new mixed acid, while (d), (e) and (f) for the conventional electrolyte.

the power required to pump the electrolyte. At a similar operating temperature, the pressure drop of the conventional electrolyte was ~6 psi at a flow rate of 0.75 L min^{-1} while that of the mixed acid was 8.3 psi even at double the flow rate, 1.5 L min^{-1}. It should be further noted that the vanadium concentration of the mixed acid electrolyte was 30% higher (2.0 vs. 1.5 M) than that of the conventional system. This advantage was attributed to the lower viscosity of the solution resulting from the chloride ion addition.

4.4. Cost benefit of advanced VRFBs over conventional VRFBs

As mentioned previously, the advanced VRFB system has potential cost benefits over the conventional system due to its ability to operate at elevated temperatures without an external heat exchanger system. A component cost model of the VRFB system was initiated to quantify the cost benefits of the advanced VRFB system and to identify dominant cost drivers and direct future research. The cost model, detailed in Ref. [17], incorporated several sub-models; 1) electrochemical performance model which takes into account flow rate effects [16], 2) shunt model, and 3) flow model considering pressure drop and pumping loss. The cost model consists of separate power and energy modules that can estimate the cost of the power and energy independently. Thus the power component cost does not include chemicals while the energy cost does not include stack and power conversion system costs. The total capital cost is obtained for the specified power and energy rating of the system. Installation cost was not included in the calculation, since it varies widely depending on if the land is

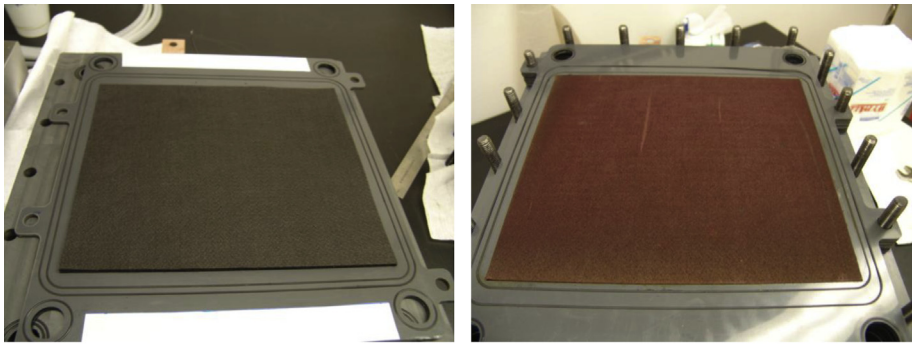

Fig. 12. Digital images of 130 cycled felt electrodes of the 3 cell stack with the conventional electrolyte: (a) negative electrode and (b) positive electrode.

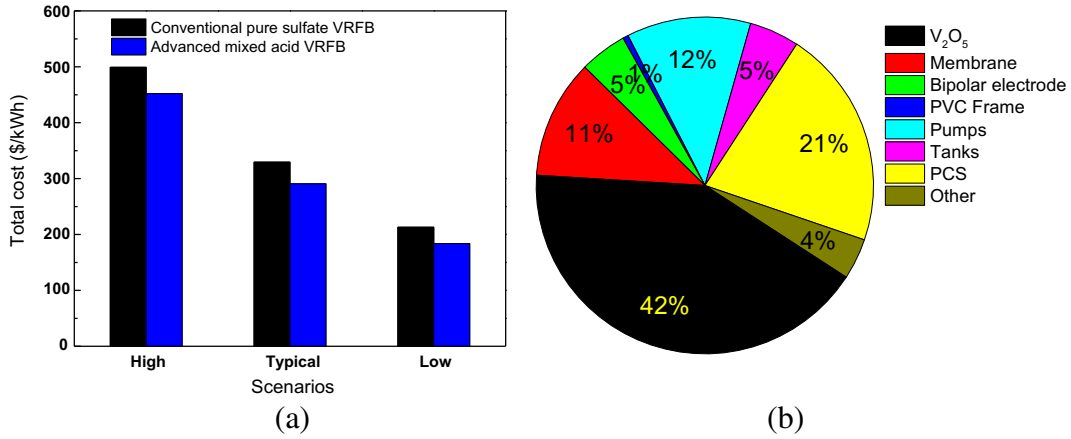

Fig. 13. (a) Total cost comparison between conventional and advanced VRFBs for 1 MW/4 MWh system (SOC 20/80%) and (b) distribution of costs and sensitivity for an advanced VRFB system.

already owned, varying regulatory requirements specific to location, and other variables. Here, the cost benefit of the advanced VRFB system over the conventional pure sulfate VRFB system is compared for a 1 MW/4 MWh system operated between 20 and 80% SOC at 1 MW.

Detailed costs for individual components were obtained from various vendors for low, moderate and high volume scenarios. The low volume scenario corresponds to high cost, and high volume scenario to low cost, with moderate volume corresponding to typical cost. Cost comparisons between the two systems are shown in Fig. 13 and show that the advanced VRFB was 10–15% more cost-effective than the conventional VRFB. For the 4-h system, chemical costs dominate (43%), while Nafion membrane cost had about half the impact. While the cost of bipolar electrode (one solid graphite plate and two porous felt electrodes) is minimal, improvement in the electrode performance would improve the efficiency and power density, thus lowering chemical and stack costs.

5. Conclusions

A 1 kW/1 kWh VRFB prototype system with the mixed acid electrolyte successfully demonstrated more than 1.1 kW over the entire operational range (15%–85% SOC) at 80 mA cm^{-2} with high energy efficiency of 82% and energy content of 1.4 kWh. The system operated stably without any precipitation at electrolyte temperatures >45 °C. At similar electrolyte temperatures, tests with a conventional sulfuric acid electrolyte suffered from precipitation after 80 cycles. By operating stably at elevated temperatures (>40 °C), the mixed acid system enables significant advantages over the conventional sulfate system, namely; 1) high stack energy efficiency due to better kinetics and lower electrolyte resistance, 2) lower viscosity resulting in reduced pumping losses, 3) lower capital cost by elimination of heat exchanger, 4) higher system efficiency and 5) simplified system design and operation.

Acknowledgments

The work is supported by the Office of Electricity (OE Delivery & Energy Reliability (OE)), U.S. Department of Energy (DOE) under contract DE-AC05-76RL01830.

References

[1] Z. Yang, J. Liu, S. Baskaran, C.H. Imhoff, J.D. Holladay, JOM 62 (2010) 14.
[2] Z. Yang, J. Zhang, M.C.W. Kintner-Meyer, X. Lu, D. Choi, J.P. Lemmon, J. Liu, Chem. Rev. 111 (2011) 3577.
[3] C. Ponce de León, A. Frías-Ferrer, J. González-García, D.A. Szánto, F.C. Walsh, J. Power Sources 160 (2006) 716.
[4] A. Price, S. Bartley, S. Male, G. Cooley, Power Eng. J. 13 (1999) 122.
[5] M. Skyllas-Kazacos, M. Rychcik, R.G. Robins, A.G. Fane, M.A. Green, J. Electrochem. Soc. 133 (1986) 1057.
[6] US Patent 4 786 567, 1988.

[7] E. Sum, M. Rychcik, M. Skyllas-Kazacos, J. Power Sources 16 (1985) 85.
[8] E. Sum, M. Skyllas-Kazacos, J. Power Sources 15 (1985) 179.
[9] US Patent 3 996 064, 1976.
[10] S. Eckroad, Technical Report, EPRI-1014836, Electric Power Research Institute, Palo Alto, CA, USA, 2007.
[11] L. Li, S. Kim, W. Wang, M. Vijayakumar, Z. Nie, B. Chen, J. Zhang, G. Xia, J. Hu, G. Graff, J. Liu, Z. Gary, Adv. Energy Mater. 1 (2011) 394.
[12] S. Kim, M. Vijayakumar, W. Wang, J. Zhang, B. Chen, Z. Nie, Feng Chen, J. Hu, L. Li, Z. Gary, Phys. Chem. Chem. Phys. 13 (2011) 18186.
[13] G. Codina, A. Aldaz, J. Appl. Electrochem. 22 (1992) 668.
[14] E.A. Kaminski, R.F. Savinell, J. Electrochem. Soc. 130 (1983) 1103.
[15] X. Ma, H. Zhang, C. Sun, Y. Zou, T. Zhang, J. Power Sources 203 (2012) 153.
[16] D. Stephenson, S. Kim, F. Chen, E. Thomsen, V. Viswanathan, W. Wang, V. Sprenkle, J. Electrochem. Soc. 159 (12) (2012) A1993.
[17] V.V. Viswanathan, A. Crawford, S. Kim, L.H. Thaller, D. Stephenson, P. Balducci, M. Kintner-Meyer, W. Wang, V. Sprenkle, J. Power Sources (2012), http://dx.doi.org/10.1016/j.jpowsour.2012.12.023.